The Thesis Committee for Jonathan Christopher Condit
Certifies that this is the approved version of the following thesis:

Laser-Induced Heating, Phase-Shift, and Damage: Measurements and Simulations

APPROVED BY
SUPERVISING COMMITTEE:

Supervisor:

Thomas E. Milner

H. Grady Rylander, III

Laser-Induced Heating, Phase-Shift, and Damage: Measurements and Simulations

by

Jonathan Christopher Condit, B.S.E.E.

Thesis

Presented to the Faculty of the Graduate School of

The University of Texas at Austin

in Partial Fulfillment

of the Requirements

for the Degree of

Master of Science in Engineering

The University of Texas at Austin

May, 2011

Dedicated to my wife Mandy

Acknowledgements

I would like to thank Dr. Thomas Milner and Dr. Grady Rylander for their support, encouragement, and endless patience with me through the years I have worked with them. It has been an honor and a privilege to be a student in their lab. I also thank Dr. Robert Thomas for his guidance, instruction, and kindness during the duration of my thesis work. Without his help this research would not have happened. I thank all those that helped with some part of this work including Gary Noojin and Kurt Schustser at Brooks Air Force Base, for advising on and helping setup experiments, Isaac Noojin for his data processing work and CD Clark for BTEC instruction. Lastly, I thank Erica Weber for Linux instruction and help with optical setup construction.

May 6, 2011

Abstract

Laser-Induced Heating, Phase-Shift, and Damage: Measurements and Simulations

Jonathan Christopher Condit, M.S.E.

The University of Texas at Austin, 2011

Co-Supervisors: Thomas E. Milner and H. Grady Rylander III

This research was a collaborative effort between the Air Force Research Laboratory (AFRL) and the University of Texas at Austin to study laser induced thermal lensing. Analysis with a high-frame rate thermal camera system in an optical cuvette determined rates of heating and cooling in water exposed to 1200, 1310 and 1318-nm wavelengths. Thermal modeling software (BTEC) developed at AFRL was used to simulate the beam parameters that were used experimentally. The simulation was also used to compute axial temperature for various power levels, beam diameters, and pulse durations. Laser-induced optical pathlength modulation or phase-shift was computed to study the thermal lensing effect. Power and irradiance damage thresholds were calculated for collimated and focused geometries to study the effect in a focusing eye on retinal damage thresholds.

Table of Contents

I: BACKGROUND

a. Overview of Related Work

Damage Threshold Study

Previously, Vincelette et al [1] studied damage and thermal lensing effects in the eye in the near infrared (NIR) wavelength region (750 nm – 1400nm) using both mathematical models and physical environments similar to the eye, including optical media, artificial eyes, and animal model eyes. Those studies included a review of producing retinal lesion study with a special focus on NIR-induced retinal damage. The studies observed the thermal lensing phenomenon in an optical media with similar physical properties to the eye, and included a mathematical model to simulate the thermal lensing effect. The studies also established NIR damage thresholds in the eye at wavelengths of 1110, 1130 and 1319nm, and used a mathematical model to predict temperature rise at the retinal plane and examine threshold conditions. Finally, the studies used an artificial eye to create a double pass optical system to observe thermal lensing and quantify the corresponding aberrations.

Findings

Thermal lensing has been documented in the literature to shift the focus of a beam of light in an absorbing optical media. Gordon and Leite [2] showed that even a weakly absorbing media could significantly shift index of refraction and thereby the focus of incident light. Since water and the eye absorb strongly in the 1300 nm range, a significant posterior focus shift is expected.

The vitreous media used was slightly denser than water but had very similar absorbance and thermal lensing properties. Therefore water is an optimal choice for simulating the vitreous media in the eye.

The first order model developed by Vincelette et al [3] provided a good fit for dn/dT values seen in a room temperature water exposure to 1313 nm laser light. The model suggests that the thermal lens effect reduces the fluence rate (W/cm^2) incident on the retina. Refractive error is observed in thermal lensing tests, where a 100-ms ED50 threshold for a 1318-nm laser causes a refractive shift of 16.44 Diopters. However, the large refractive shift still did not circumvent retinal damage from the 1318-nm laser, raising questions about the role of thermal lensing in damage prevention.

The study model showed that for large beam diameters, the power required to reach a retinal damage threshold varied by up to 28% between cases with and without thermal lensing. Vincelette further stated that 28% may not be significant due to the biological variability under a larger beam diameter. Chromatic dispersion may also account for some of the thermal lensing in the model by overestimating beam-waist radius at t=0. Results suggested that the retinal ED_{50} for small diameter beams is greater than 14.5 W at 1319-nm for an 80-ms exposure.

Thermal lensing involves higher order aberrations beyond defocus and astigmatism. Vincelette suggested that an adaptive optics technique could be used in animals to investigate thermal lensing in-vivo as long if exposure conditions remain below damage thresholds.

Future Studies

The dissertation explored thermal lensing and retinal damage thresholds, with minimal attention to corneal damage (other than a reference in section 1). Corneal damage is important to understand corneal safety thresholds. This thesis examined some questions that were unanswered by the Vincelette dissertation. First, corneal damage thresholds were examined by looking at shallower depth thermal effects. At near IR laser wavelengths (eg, 1319 nm) and short laser pulse times (less than 0.1 s), the retinal damage threshold is lower than the corneal damage threshold. For longer pulses, (between 0.1 s and 1.0 s), the corneal damage threshold becomes lower than the retinal damage threshold. Longer pulse durations were used in the thesis work to examine

corneal damage thresholds and gain understanding about the tradeoff between the retinal-corneal damage threshold transition.

Second, the thesis will further explore the focusing geometry and effects of the eye on incident light. The retinal-corneal damage threshold transition is also dependant on the focusing geometry of the eye. The thesis examined where the damage threshold occurred in a focusing geometry. As optical power increases (focal length becomes shorter), the peak irradiance increases. Irradiance decreases with strong absorption.

DPOCT Phase-Shift Measurements in Laser Pulsed Media

Kim et al used differential-phase optical coherence tomography (DPOCT) to investigate short-pulse laser-induced optical path length change by accounting for refractive index change and thermal expansion induced variation. A polarization-maintaining DPOCT system measured through a sample-holder filled with a dye solution that absorbed in the visible, with a peak at 585 nm. The container was configured in a unconstrained (open top) and constrained (filled, sealed top) geometry. A flash-lamp pumped pulsed dye laser irradiated the source at short pulse durations (400 to 500 us) and a range of energy levels to observe shifts in the optical path length and thermoelastic expansion using DPOCT.

Findings

A laser-induced temperature increase was achieved in both the confined and free space geometries. In observing the differential phase change, the constrained geometry path length decreased due to thermorefractive change. The free geometry path length was governed by both thermorefractive and thermoelastic change, and increased due to the thermoelastic effect being stronger than the thermorefractive effect for the given energies, pulse durations and optical/thermal properties of the media. The change in refractive index with temperature, dn/dT, values were obtained using a linear curve-fitted temperature dependence term, C1. The measured dn/dT was nearly twice the value given by the National Institute of Standards and Technology (NIST). This difference was attributed to lateral thermal expansion of the dye solution.

Future Work

The study concluded by expressing the need to make further measurements with larger beam diameters and powers in order to achieve better agreement between a measured dn/dT and the value given by NIST. In this thesis, small and large beam diameters were used, as well as longer pulse durations. A computational model was used to examine dn/dT with a larger beam diameter and higher incident fluence. The model was also used to compute phase shift (optical path length change) as a function of focusing geometry, initial beam diameter, wavelength and power.

b. Anatomy, Geometry, and Optical Properties of the Eye

A partial goal of the thesis was to understand better aspects of laser interaction with water as a model of the eye. Therefore, gaining an understanding of the basics of anatomy, geometry, and optical properties of the eye is necessary.

The eye is globe-shaped, with a protrusion on the anterior (front) surface due of the eye. The front surface protrusion, known as the cornea, has a smaller radius of curvature than the rest of the eye, acting as the first optical element in a multi-element lens system. Each component has a different tissue composition and therefore different optical properties. Below (Figure 1) is a figure in the human eye, with various layers and corresponding human thicknesses and absorption coefficients.

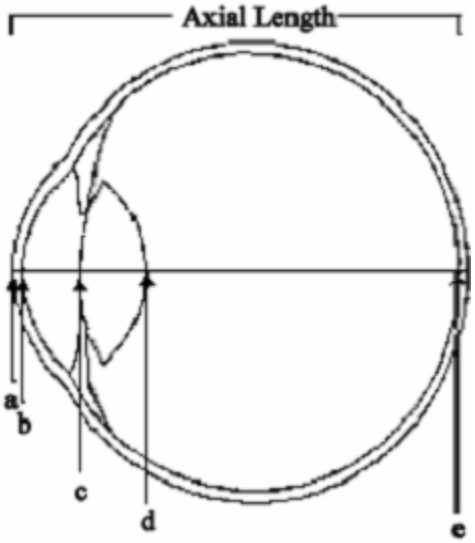

Figure 1: Human Eye Layers [5]

Layer	Name	Thickness (cm)	Absorption @ 1318-nm (cm^{-1})
a-b	Cornea	0.05	1.51
b-c	Aqueous Humor	0.31	1.22
c-d	Lens	0.46	0.61
d-e	Vitreous Humor	1.72	1.13

Table 1: Properties of the human eye at 1318 nm [6]

c. Applications of near IR light, importance of damage threshold measurement

The Near Infrared (NIR) is a useful radiation band for therapeutic heating and imaging of the eye tissue due to the scattering and absorption properties of tissue in this band. Therapeutic applications include laser-tissue welding [7], while imaging applications include optical coherence tomography (OCT), a high-resolution cross-sectional imaging modality used in shallow epithelial tissues and retinal imaging. Since the NIR is a commonly used radiation bandwidth, it is important to understand damage thresholds in the eye to protect operators, patients, and subjects present during the use of NIR wavelength light.

d. Objectives

The Kim study concluded by expressing the need to make further measurements in order to achieve better agreement between a measured dn/dT and the value given by NIST. This thesis studied experimentally and computationally the temperature increases under radiation by small and large beam diameters, and utilized a computational model to examine dn/dT and phase shift. Vincelette's dissertation studied thermal lensing and retinal damage thresholds, with minimal attention to corneal damage. The retinal-corneal damage threshold transition is dependant on the focusing geometry of the eye. The thesis examined where the damage threshold occurred in a focusing geometry versus a collimated geometry.

Objective 1: Characterize thermal response of water in near IR wavelengths between 1.1 and 1.4 microns

The first objective of this thesis was to study and characterize the thermal response of water, which is a model for the aqueous humors of the eye, in the Near Infrared optical range between 1.1 μm and 1.4 μm. The characterization was achieved experimentally and computationally. A thermal camera was used to observe a series of pulses of different wavelengths, beam diameters, and pulse durations on different water thicknesses, representing different depths in the eye. Experimental parameters for the beams and the media were input into a photo-thermodynamic computational model called BTEC (an acronym for the last names of the primary contributors to the code).

Objective 2: Utilize BTEC model to simulate phase shift and focus effects on damage thresholds

The second objective was to utilize the BTEC photo-thermodynamic model in water as a representation for the aqueous humors of the eye. The change of refractive index given by the computational data was computed from the experimental parameters, and the deviations were examined and analyzed. Damage thresholds were computed based upon beam diameters and wavelengths used in the experiment, using collimated and focused geometries.

II: Theory and Principals

a. Physics of Photothermal Response

Photothermal interaction occurs when a light source is incident upon a medium that absorbs photons at the wavelength of the light source. Photothermal interaction in optically clear media such as water or corneal tissue is governed by a number of factors, including scattering, absorption and transmission properties of media and the wavelength, energy, exposure duration and spatial distribution of the light. When photons incident on a media are absorbed, radiant energy is transferred to thermal energy in the media. This energy transfer, and subsequent thermal processes are governed by the thermal properties of the media and include specific heat, conductivity and convective heat transfer coefficient at the surface.

Radiant flux φ is a measure of total optical power, either leaving a source or impinging upon a surface. Radiance L describes the amount of light passing through a surface or medium, at a certain incident angle and falling within a specified area A and solid angle ω. Radiance is given as

$$L = \frac{d^2\varphi}{d\omega} dA \cos\theta \qquad \text{Eq. 1}$$

where phi is the flux, omega is the solid angle, A is the emission or collection area of the beam, and theta is the angle between the surface normal and the direction of radiation.

Radiative transfer equations govern the transport of light through media, but the full equations are typically not solvable in closed form. Therefore, approximations for absorption-dominated and scattering-dominated regimes can be used. In the case of an absorbing media such as water or corneal tissue, the radiance can be described by a modified Beer's Law:

$$L = L_0 e^{(-\mu_t z)} \qquad \text{Eq. 2}$$

Where z is depth in the media and μ_t is the extinction coefficient, the sum of μ_s and μ_a, the scattering and absorption coefficients, respectively.

As photons are absorbed by the media, the light energy is converted to thermal energy in the media. The absorbed power of the beam per unit volume is the product of the beam irradiance and the medium absorption coefficient. This term, known as the source term Q, can be used to solve the temperature increase in the media by using the non-steady heat conduction equation:

$$\rho c_p \frac{\partial T}{\partial t} - \kappa \nabla^2 T = Q \qquad \text{Eq. 3}$$

where ρ is the density of the medium, c_p is the specific heat at constant pressure, T is temperature, and κ is the thermal conductivity. Therefore, temperature increase of media under photonic radiation can be predicted with the thermal and optical properties of the media and the radiance of the source.

b. Physics of Thermal-Induced Phase Shift

When laser radiation heats a media, the temperature change gives rise to a change in refractive index. This effect has been called thermal lensing [8]. The error introduced to the expected propagation (without thermal lensing) is known as the phase error ϕ. To calculate the effects of thermal lensing in a media heated by laser, an optical path length change $\delta(T)$ is computed by integrating the temperature-dependent refractive index $n(T)$ over the axial direction z:

$$\delta(T) = \int_{z_1 T}^{z_2 T} n(T) dz \qquad \text{Eq. 4}$$

After calculating optical path length change, the phase error ϕ can be computed as:

$$\phi = \frac{4\pi}{\lambda} \delta(T) \qquad \text{Eq. 5}$$

where λ is the wavelength of the incident beam.

c. Principals of the BTEC Computational Modeling Software

The BTEC thermal model [9] is a simulation developed to create computational models of optical radiation and radio frequency thermal interaction with tissue. The code was selected to model the experiments described in this thesis because of its robustness and flexibility in simulating laser propagation, heat transfer, refractive index change with temperature, and combined effects of laser propagation and heating. BTEC also has capabilities to compute tissue damage and damage thresholds.

Heat Source Creation

The heat source term from the irradiation beam is an input into the heat conduction equation for modeling the thermal diffusion over time. The heat source can be arrived at in two ways: first, through the Monte Carlo simulation, and second, by using Beer's law.

With the Monte Carol approach, a weight assignment is given at each grid point proportional to the weight decrease of the photon packet at each scattering location. This weight assignment represents the energy absorption of the media. The photon densities at each grid point can be integrated to arrive at the source term in the heat equation (Eq. 5). BTEC can also compute a source term based on the beam profile (e.g., top-hat vs. Gaussian) and absorption using Beer's law.

BTEC uses a finite difference numerical method to solve heat transfer using a Crank-Nicholson method in the 2-D solution. BTEC is configured by using a source file to specify the energy source, layer files to represent water and container, and sensor files to read out changes in temperature, energy or other properties at desired locations. A series of initial conditions and settings to describe boundary conditions, time step and other properties are set before running the model.

BTEC damage calculation

BTEC can perform damage calculation and damage threshold searches using an Arrhenius first-order rate equation,

$$\Omega(z,r,\tau) = C\int_{t1}^{t2} e^{\frac{-E}{RT}} dt \qquad \text{Eq. 6}$$

where omega is the normalized damage threshold, R is the universal gas constant, C is a normalization rate constant and E is activation energy. BTEC uses a standard rate process model for thermal damage or can search for a given temperature.

III: Experimental Design

a. Experimental Systems

An experimental system was constructed to observe response of water to IR irradiation (1200, 1310 and 1318-nm). The system was a thermal camera-based system and was constructed to measure water temperature as a function of time before, during and after a shuttered pulse of laser irradiation. The system was built with two different laser excitation sources, with different wavelengths and output powers. The first system configuration had an adjustable wavelength light source (Mira-OPO PP Automatic IR-S1-830 fs, Chameleon Ultra II pump, APE Coherent, Santa Clara, California) of limited power output. The second system configuration had a fixed-line (Nd:YAG, 718T, Lee Laser, Orlando, Florida) source with a significantly higher power output level that was attenuated to desired levels.

Thermal Measurement System

In addition to the IR laser sources, the system (Figure 2) consisted of a thermal camera (SC6000 camera, FLIR Systems, Wilsonville, Oregon), beam-directing mirrors (1310 nm peak reflection, y13-1310-45-P, CVI Laser, LLC, Albuquerque, New Mexico) a shutter (Uniblitz VMM-T1, Vincent Associates, Rochester, New York) and a water-containing cuvette with an optical window (or "well plate"), and in the 1318 nm system configuration, a half wave plate (WPH05M-1310, Thorlabs, Newton, New Jersey) and beam splitting polarizer (CM1-PBS254, Thorlabs) to attenuate the beam . The water-containing cuvette was mounted such that a beam entered normal to the well plate on the bottom surface of the cuvette, passed through the water, and exit from the top surface of the water. This geometry allowed the camera, positioned directly above the cuvette, to measure the temperature increase on the exit, or "back" surface of the water. This measurement configuration allowed parallels to be drawn between the back surface of the water and temperature increase at various depths in the eye.

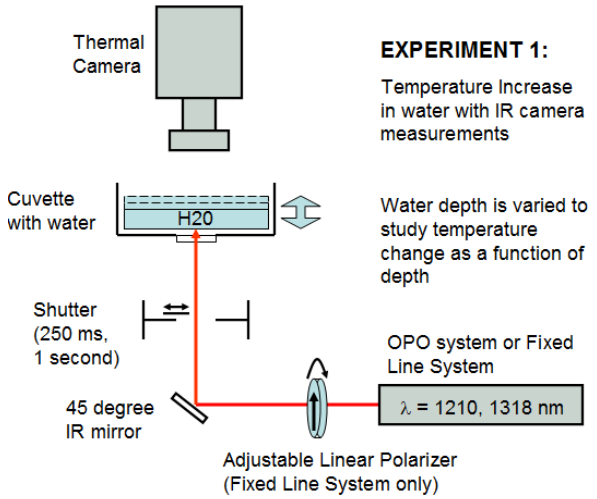

Figure 2. Thermal camera setup for temperature rise measurements under near-IR laser pulses

The OPO source was a tunable wavelength laser. 1200 and 1310-nm wavelengths were used, with beam diameters of 5 mm and 2 mm, respectively. Between 700 and 800 mW were measured at the source. The Lee Laser IR source was an Nd:YAG laser, with wavelength 1319 nm, spot size 3.2 mm and output power of 3.0 W measured at the source. Both laser sources were well collimated over the length of the optical table.

The mirrors were round 28 mm mirrors with a coating for high reflectivity in the IR wavelength range. The cylindrical cuvette had a diameter of 25.4 mm, a depth of 8.0 mm and a well-plate with a diameter of 10 mm in the center. The thickness of the polycarbonate well plate was 0.02 cm, with a refractive index of n = 1.58. Deionized water (n = 1.34) was used as an absorbing media in the cuvette. The camera frame rate was 800 frames per second, and each capture was set to 3200 frames, or 4 seconds of video. The recorded frames were 192 pixels by 192 pixels in dimension. The camera view area was spatially calibrated by imaging a mm-scale ruler. The viewable area was 25 mm by 25 mm, with pixel dimension of 7.5 pixels/mm. The camera was calibrated by using a Mikron blackbody heat source so that the dynamic range of each pixel was 15-45 degrees C.

b. Method for Temperature Rise and Refractive Index-Shift Experiments

After constructing the experimental setups, calibration and measurements were performed, followed by experimental runs and data capture. Because an objective of the thesis was to compare the agreement of experimental measured data to simulated values from computed models, careful calibration of the equipment was vital to maximize the accuracy of the measured data, and to measure carefully the characteristics of the beam and the targets to maximize the authenticity of the simulation inputs.

Thermal Camera Temperature Calibration

Before recording measurements, the thermal camera was calibrated with a Mikron blackbody source (M345X8, Mikron, Oakland, New Jersey). First, the thermal camera was used to acquire an image of a temperature-monitored reference plate. Gain and offset were set in the camera software as an initial calibration. Next, two upper and lower bounding temperatures (15 degrees C and 45 degrees C) were set with the blackbody source to achieve non-uniformity correction (NUC). Non-uniformity correction helps smooth out the variation in measured surfaces due to bad pixels in the detector array, noise, or other factors. After setting the NUC, a range of temperatures spanning the bounding temperatures were set on the blackbody and acquired on the thermal camera. The step size of these temperatures was closer across the expected range of temperature increase under laser irradiation. Finally, the calibration was tested by moving the blackbody across the range of temperatures, setting different temperature points than those used in calibration, and reading average temperature in the viewable area acquired by the thermal camera. The calibration values and test values are shown in Table 2.

Ambient Temp	Reference Plate Temp	Reference Plate Counts	Blackbody Temp (set)	Blackbody Temp (actual)	Blackbody Counts
19	20	5085	15	15	4035
19	20	5125	18	18.02	4746
19	20	5136	22	21.97	5780
19	20	5190	25	25.03	6655
20	20	5200	28	28.04	7562
20	20	5225	31	30.99	8600
20	20	5267	35	35.08	10081
20	20	5300	40	40.1	12185
20	20	5345	45	45	14540

Table 2: Thermal camera calibration data

Excitation Laser Beam Spot-Size Measurement

The output power of the excitation lasers were measured using a wide area detector power meter. The spot size was measured by using a knife-edge measurement technique, in which a razor edge mounted on a micrometer stage was advanced through the beam and power level drop is measured. First, the beam was exposed onto a power meter, so that full power was measured. Next, the razor was advanced in a plane perpendicular to the axis of the beam through the beam until the power dropped to 85% of the maximum power. At this point, the micrometer position was recorded, and the razor was further advanced through the beam until the power meter read out 15% of the beam maximum power. The micrometer position was again recorded, and absolute value of the subtraction yields an approximation of the beam width. A beam expander (2X expander, BE02M-C, Thorlabs, Newton New Jersey) was put into the beam path, and the measurements repeated.

The beam power was initially measured at a power of 2.0 Watts, and the 85% and 15% intensity values were displaced by 1.9 mm. After placing the beam expander in the path

of the beam, the power level was reduced to 1.85 Watts, and the 85% and 15% intensity values were displaced by 5.0 mm. A $1/e^2$ value calculated the beams at 3.2 mm and 10.2 mm diameter.

Method for Thermal Camera Radiometric Temperature Measurements

The method for radiometric temperature rise experiments was to expose shuttered laser pulses of 250 ms and 1 second to depths of water of 2.2 mm to 6.6 or 7.7 mm and measure the temperature increase and relaxation as a function of time using the thermal profile for each pulse duration and depth. The power levels, wavelengths, and laser spots sizes used, as well as water depths, are given in Table 3.

	Configuration 1: OPO		Configuration 2: Fixed-line	
Wavelength	1310	1200	1318 nm	1318 nm
Beam Diameter (1/e)	2.0 mm	5.0 mm	3.2 mm	10.1 mm
Power Levels	550 mW, 500 mW	535 mW, 400 mW	2.0 W	1.85 W
Exposure Times	250 ms, 1 s	250 ms, 1 s	250 ms, 1 s	250 ms, 1 s
Water Depths	2.2, 3.3, 4.4, 5.5, 6.6 mm	2.2, 3.3, 4.4, 5.5, 6.6 mm	2.2, 3.3, 4.4, 5.5, 6.6, 7.7 mm	2.2, 3.3, 4.4, 5.5, 6.6, 7.7 mm

Table 3: Beam properties, exposure times, and water thicknesses for thermal camera measurements

The setup was first constructed around the adjustable-wavelength OPO laser. After the setup was built, the cuvette was placed in the imaging field of the thermal camera, and 2 mL of water was added to provide a depth of 2.2 mm. The camera vertical position was adjusted to focus on the top surface of the water-containing cuvette. A thermal camera recording acquisition was initiated, followed by opening of the laser shutter for 250 ms.

The total thermal camera acquisition time was 4 seconds, which included time before, during and after the excitation laser pulse. After laser excitation, the acquisition recording was played back to ensure that then entire duration of the pulse and thermal relaxation region were recorded. The acquisition and shuttering process was repeated at least one additional time, to verify the entire duration of the pulse and thermal relaxation region were recorded

The shutter open time was then increased to 1 second, and at least two thermal camera acquisitions were recorded of the radiometric temperature increase in water and thermal relaxation at that shutter open time. After video acquisitions at the two different shutter open times, 1 mL of water (1.1 mm depth) was added to the cuvette, for a total volume of 2 mL and depth of 2.2 mm of water. Radiometric temperature of pulses at the two different shutter exposure times were acquired, recorded by the camera and played back to insure quality and completeness of the recorded data. This process was repeated for the addition of each 1 mL of water, one mL added per acquisition set, until the cuvette was full at 6mL. Each mL of water added 1.1 mm of depth to the cuvette.

After a full set of thermal camera acquisitions were made at two different exposure times and 5 different depths (2.2, 3.3, 4.4, 5.5, 6.6 mm), a Thorlabs beam expander was placed into the path of the beam. The beam diameter increased from 2 mm to 5 mm. The experiment was repeated with the new beam diameter, stepping through each depth from 2.2 mm to 6.6 mm in 1.1 mm increments with 250 ms exposures and 1 s exposures. At the time of measurement, the ambient temperature was 20 degrees C.

Following this set of experiments with the OPO laser, the system was torn down and rebuilt at another optical table with a 3 Watt single line LEE laser at 1318 nm. This system power, with a 2 mm spots size, was such that it was necessary to attenuate the beam to 2.5 Watts to avoid damaging components. A half-wave plate and polarizer were used to attenuate the beam. The power at the well plate surface was 2 watts before putting the beam expander in place. The complete experiment above was duplicated with the new laser source. The extra power in the system allowed for an extra mm of depth to be

added, with depth measurements spanning from 2.2 mm up to 7.7 mm in 1.1 mm increments, rather than 6.6 mm. The beam expander increased the beam diameter from 3.2 mm to 10.2 mm, and the power dropped from 2 W to 1.85 W for a 7% loss through the system. It should also be noted that due to an air conditioning outage, the ambient temperature for the second configuration (single-line 1318 nm source) was 27.5 degrees C, or 7.5C warmer than the previous experiment.

c. Initial Conditions and Input/Output parameters of Simulation

The BTEC computational model supports a large number of initial conditions and parameters representing the material, time-step, geometric and dimensional properties. Initial conditions and input/output parameters were selected to represent the physical geometries and properties of the thermal response system and optical system responses.

Emitter

The emitter type was selected as a "LinAbsEmitter", or Linear Absorption Emitter, meaning it assumes Beer's Law Absorption along the propagation direction. The beam profile was set as "top hat", meaning that the energy was input equally over a given diameter, and was zero outside the diameter, with no roll-off. The peak power, minimum wavelength, and beam diameter were varied based upon desired source to simulate. Beam waist was set at zero. Pulse Duration, Start, and Stop time and Time Step were also set. Pulse duration was set according to the experiment we were simulating. The pulse start time was immediate, rather than delayed as in the measured data, for convenience when analyzing and stop was also set in accordance with the total acquisition time of the camera. Time step was set in the millisecond range to simulate the high frame rate of the thermal camera.

Layers

The cuvette and water material properties were input into the BTEC as layer files. The cuvette layer used a "well plate" of thickness value of 0.02 cm, density of 2.51 g/cm^3,

specific heat of 0.858 J/g/degC, conductivity of 0.0114 J/s/cm/degC, and convective heat transfer rate of 0.0005 J/s/cm2/degc. The refractive index, absorbance and scattering constants of water were drawn from BTEC data tables as a function of wavelength.

The water layer used thickness values of 0.22 cm, density of 1.0, specific heat of 4.1868, conductivity of 0.00628 J/s/cm/degC, and convective heat transfer rate of 0.0015 J/s/cm2/degc. The refractive index, absorbance and scattering constants were also drawn from a BTEC data table as a function of wavelength. The full set of layer values for water and the cuvette window material are given in Table 4:

	Density g/cm^3	Specific heat J/g/degC	Conductivity J/s/cm/degC	convective heat transfer rate J/s/cm2/degc
Water (DI)	1.0	4.1868	0.00628	0.0015
Cuvette Optical Window	2.51	0.858	0.0114	0.0005

Table 4: Physical, mechanical, and thermal properties of water and cuvette layers used in the BTEC computational model

Sensors

Temperature sensors were set along the grid such that back temperature, front temperature, and uniformly spaced temperature locations throughout the depth were output as a function of time. Axial temperature of the entire depth were also logged at uniform 50 ms timesteps, providing time snapshots of the axial temperature profile.

Thermal Lensing: Phase shift

BTEC was used to model temperature-dependant refractive index change (dn/dT) in water to study thermal lensing effects present in the eye and other absorbing media. Similar beam parameters used in the thermal measurement experiments were input into

the phase model. The refractive index change can be integrated over depth to find optical path length $\delta(T)$, which is then used to solve for phase shift ϕ, as seen in equation 5.

Damage Threshold Calculation

BTEC was used to compute damage thresholds using the Arrhenius damage integral equation. The target geometry was represented within the model both single planar layer of water with a collimated beam, and as a focusing layer of water. The damage model was run for exposure times between 0.1 ms and 1 second, corresponding to previous experimental measurement times. Geometric and thermal lensing effects were also accounted for in the activation energy term.

IV: Results

a. Results of Temperature Rise Experiments

The data collected from laser temperature rise experiment was a series of thermal camera .MOV movie files. Each pulse was preceded by 500-1000 frames (0.625 – 1.25 seconds) showing water at ambient temperature, followed by a 250 ms (200 frames) or 1 second (800 frames) laser pulse, followed by 1400-2450 frames (1.75 – 3.1 seconds) of temperature delay. A colorized camera image frame corresponding to a 1s pulse duration and 3.2 mm beam diameter runs are shown below.

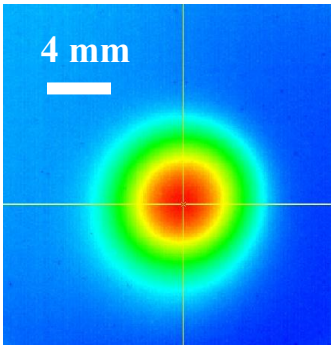

Figure 3: Colorized thermal camera video frame. 1 second pulse of 1318-nm light at 2 Watts power, 3.2 mm beam, frame taken 2 seconds following pulse, 2.2 mm water thickness

Image and Data Processing

To analyze the results of the temperature rise and refractive index shift experiments, image processing was performed using Labview and Excel was used to plot and display data. For each thermal camera video, a region of interest (ROI) was selected centered around the beam center to allow for temperature averaging of the region of water where the beam was incident. The temperature average for the region of interest was calculated for each frame, giving a time-temperature average curve for each set of water depths and beam exposure times. The maximum temperature in the region of interest was also logged for each frame, so that a time-temperature maximum curve for each set of water

depths and beam exposure times could be generated. Finally, maximum and average temperatures were also recorded for each depth, so that an axial time-temperature maximum and average plots could be generated.

The average and maximum time-temperature histories at certain depths can be seen below in Figure 4. Figure 4a shows the average temperature in a selected region of interest. A rapid temperature increase is observed during laser irradiation, followed by a diffusion of heat to the surrounding media and top and bottom boundaries. Ripples seen in the temperature profile may be due to a small region of interest that did not always encompass the heated area, or ripple-like movement of the surface of the water. Figure 4b show maximum temperature in a region of interest at various depths of water, starting at 2.2 mm and moving up in 1.1 mm increments to 5.5 mm.

(a) (b)

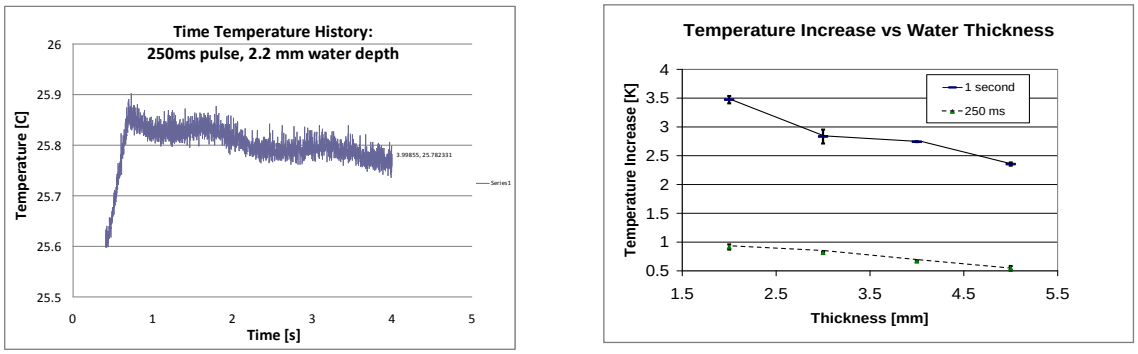

Figure 4. Thermal camera measured data. a) Thermal camera-recorded time-temperature history of top surface of the water cuvette. b) Temperature increase at each depth, for 250-ms pulse.

b. Results of Computational Models

BTEC software was used to generate computational results for comparison with the measured results. Temperature increase was computed axially over time. Maximum

temperature was computed for various pulse durations, beam diameters, power levels and water depths. Measured data was plotted against computed data to validate model and evaluate differences. Change in refractive index was computed with temperature change, and integrated over depth to find optical path length difference, which was used to compute phase shift over time to study the thermal lensing effect. Finally, damage levels were computed to identify thresholds.

Computed and Experimental Maximum Back Temperatures

Maximum back temperature for different pulse durations, power levels and spot sizes were computed. These measurements were most suited for directly comparison with experimental results. Shown below are computational results of various parameters, followed by plots of measured data against computational data. Figure 3a (left) shows maximum back temperature increase for a 250 ms pulse, and Figure 3b (right) shows 1 s pulse. The temperature increase was linear with pulse duration. The measured data of Figure 5 and the computed data is plotted together to show the fidelity of the model are shown below in Figure 6.

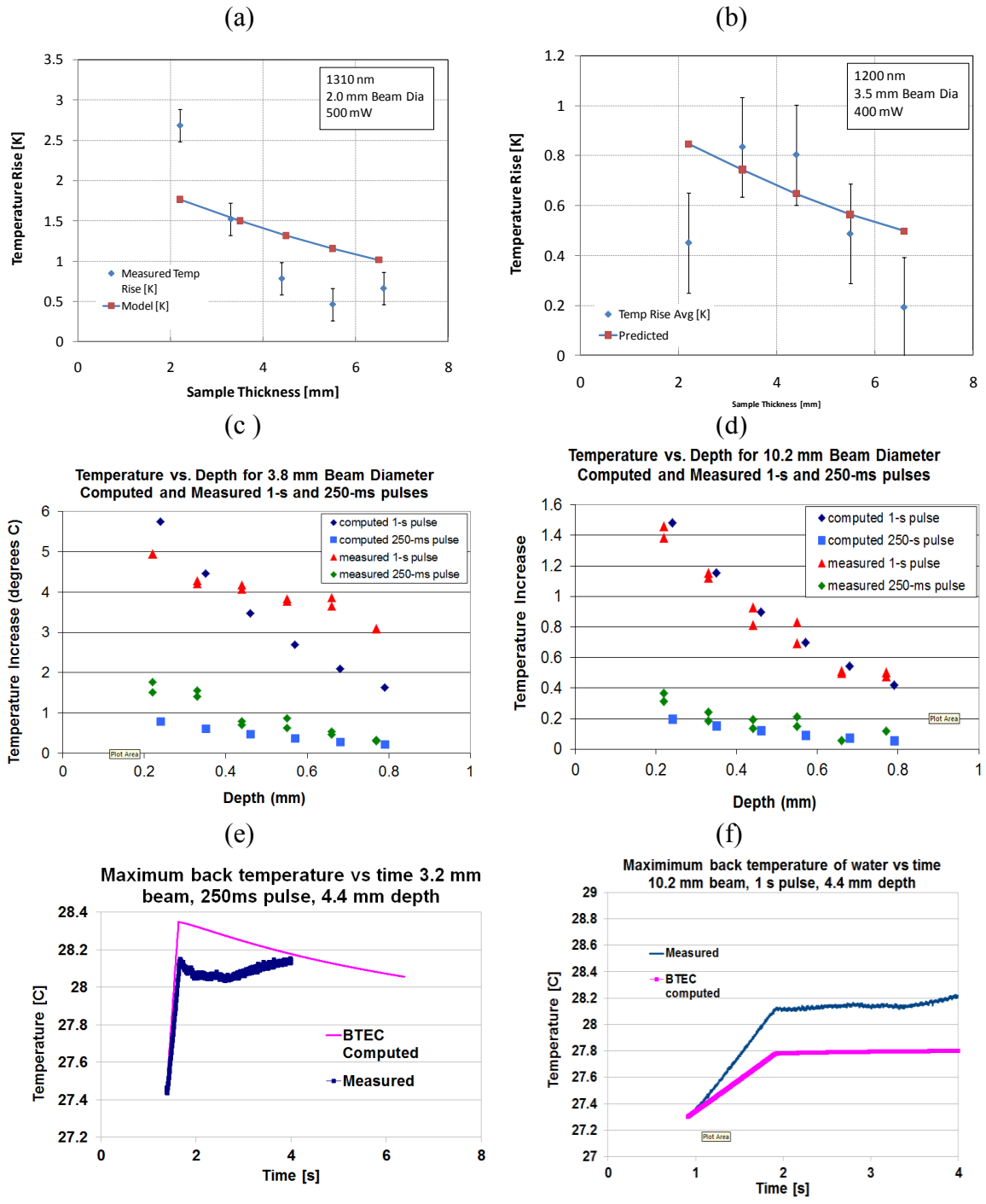

Figure 5. Measured and Computed thermal data. Figures a) and b) show back surface average temperature rise vs. depth at 1310 and 1200-nm, respectively. Figures c) and d) show back surface average temperature rise vs. depth at 1318. Figures e) and f) show maximum back temperature vs. time for a 4.4 mm thick water sample.

Axial Temperature Change vs. Time

When a water sample was measured with a thermal camera, radiometric temperature at only one depth could be measured at a time since the camera was looking at the back surface of the water. The BTEC computational approach had the advantage of being able to predict temperature at every depth level along the axis of the beam, at any given time. These snapshots in time were plotted together to demonstrate the axial temperature profile variation over time.

(a)

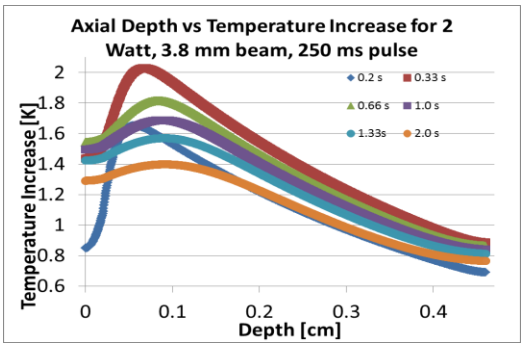

(b)

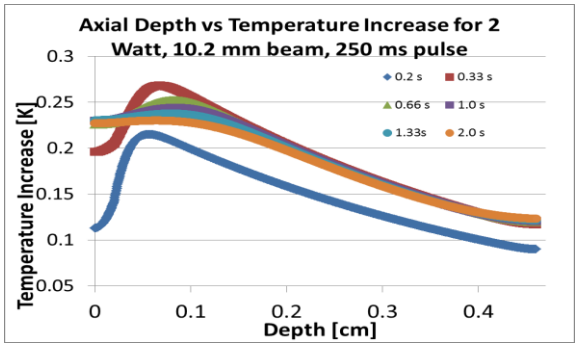

(c)

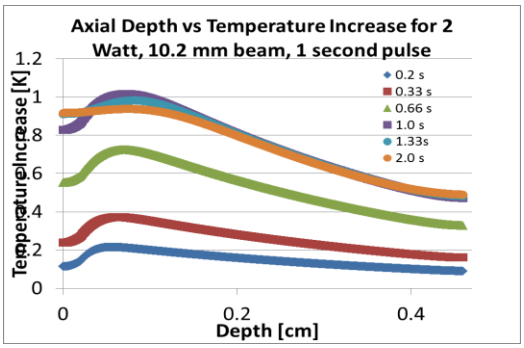

(d)

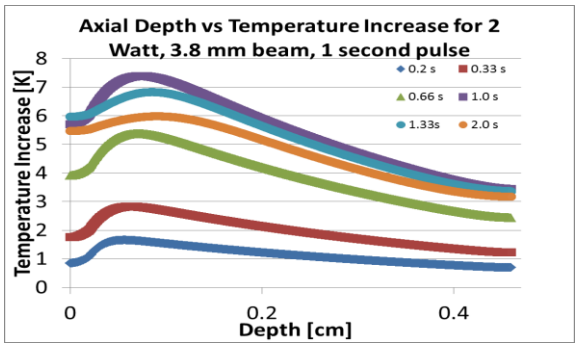

(e)

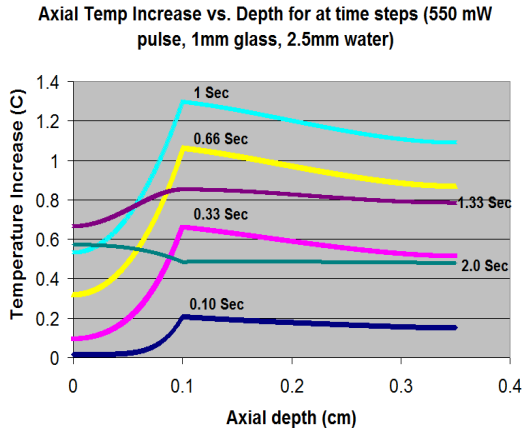

Figure 6: Axial temperature rise over time. Axial temperature rise was computed for the various beam input parameters. These computations showed axial temperature distribution in water at various snapshots in time. Figures a)-d) were higher power cases at 1318 nm and 2 Watts and Figure e) was created for lower power cases at 1310 nm, and 550 mW.

dn/dT and Phase Shift

To study thermal lensing effects, the change in refractive index over the axial depth was computed for various beam parameters. By integrating the refractive index over the axial depth of the sample, from top surface to bottom surface, an optical path length difference due to laser irradiation can be computed, from which phase changes may be computed for different power levels at different thicknesses.

(a) (b)

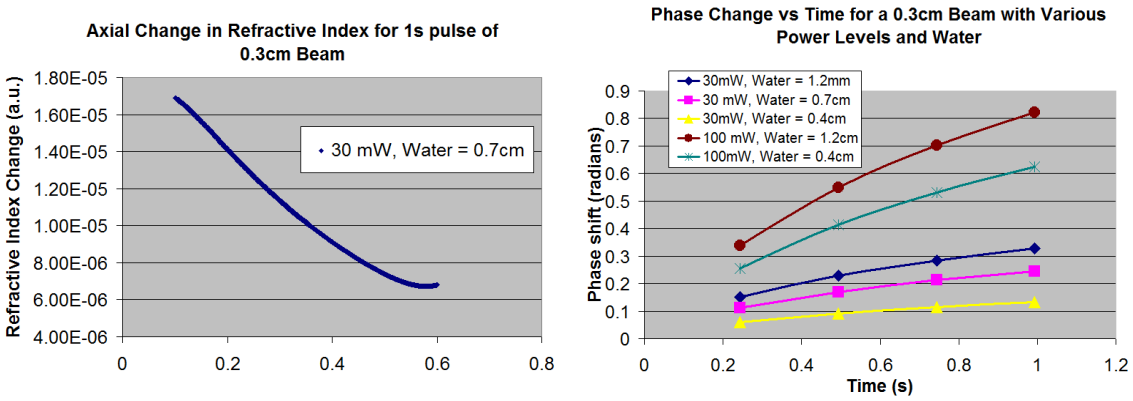

Figure 7. Refractive index and phase change. a) Axial change in refractive index with depth. b) Phase change with various power levels.

Damage Threshold Calculations

To study the effects of thermal lensing on damage thresholds, a computational model was run with similar beam diameters and pulse durations for a collimated and focusing geometry. Power and irradiance thresholds were examined as a function of pulse duration and beam diameter for the collimated and focused geometries. Results are shown below in Figure 9.

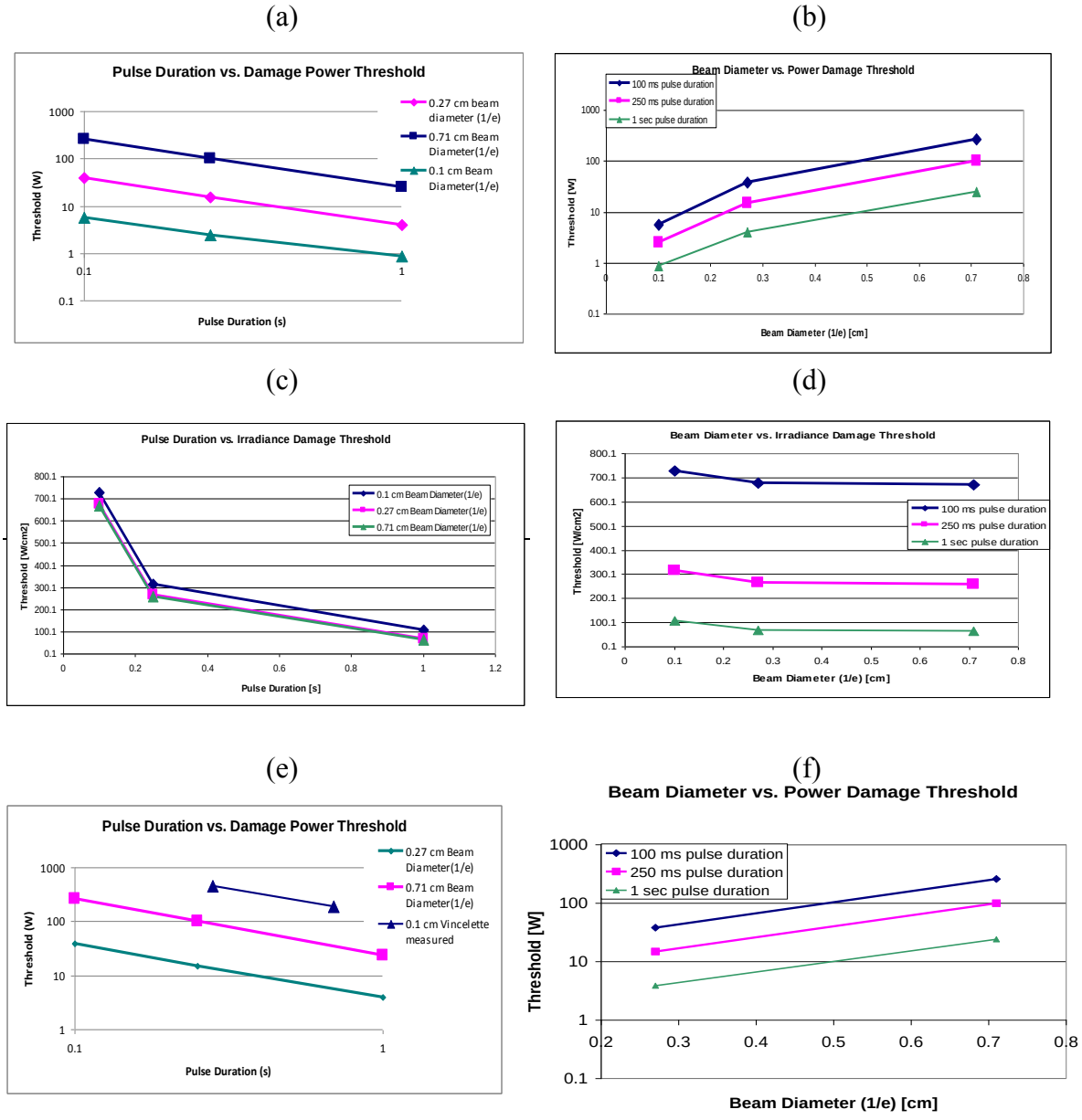

Figure 8: Damage thresholds for collimated and focused geometries. a) - d) Damage thresholds vs pulse duration and beam diameter, collimated geometry. e) - h) Damage thresholds vs. pulse duration and beam diameter, focused geometry.

(g) (h)

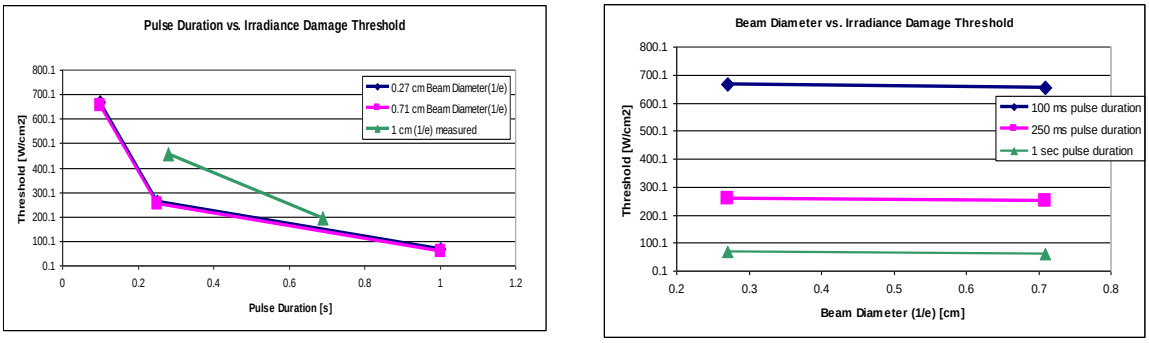

Figure 8: Damage thresholds for collimated and focused geometries. a) - d) Damage thresholds vs. pulse duration and beam diameter, collimated geometry. e) - h) Damage thresholds vs. pulse duration and beam diameter, focused geometry.

V: Discussion

Measured temperature vs. thickness (Figure 5a-d) dropped off as thickness increased, consistent with modified Beer's law governing the absorption, where radiance falls off as exp^(-μ_az). The measured vs. computed temperature showed some disagreement in the thinnest water samples (< 3.5 mm). Measured temperature was greater than computed values. Multiple reflections from the water-cuvette interface may have resulted in additional heating of the air-water interface. The small water volume (2 mL, 3 mL) in the cuvette was subject to surface tension effects on the side walls. The meniscus on the top surface varied from sample-to-sample and was a possible source of variation between the measured and computed data. Another source of error was that since the shutter was close to the sample and was being heated by the laser after closing, radiant emission from the shutter may have introduced an artifact in measured radiometric temperature. The laser settings that showed the greatest temperature increase were those with the highest pulse duration, greatest power, and smallest spot beam spot. Those levels corresponded to a 1 second pulse, 3.2 mm beam spot, and 2 Watts of power.

The thinnest water samples also showed the greatest temperature increase due to the least amount of thermal diffusion. Marked temperature rises were observed in the water following laser irradiation in all but a 250 ms pulse duration in 6.6mm or greater water depths. As the laser beam propagated through the media, energy was absorbed according to Beer's law. The amount of energy absorbed as a function of depth falls off exponentially. At a sufficient depth, most input energy is absorbed. The energy absorption through 6.6 mm of water was such that no temperature increase was measured on the back surface of the water by the thermal camera.

The computed data (Figure 5 c,d) fit well with both small diameter (3.2 mm) and large diameter (10.2 mm) beams. Variation in room temperature may have contributed to divergence of the small beam 1 second pulse. The computed large beam diameter fit very

well for both the 1 second and 250 ms pulse. The model appears to perform best at lower temperature rises.

The maximum back surface temperature as a function of time was highest temperature point in a measured region of interest on the back surface of the water through the extent of the thermal camera video capture. The measured maximum back surface temperature data (Figure 5 e,f) showed a decrease, then flattening of the thermal diffusion. This measurement was taken at a thickness of 4.4 mm so temperature decrease is slower due to a larger volume. The computed maximum back temperature fits very closely in temperature, with an initial discrepancy of less than 0.5 degrees C.

Temperature rise as a function of axial temperatures can be seen in Figure 6. Beam profile size, by increasing irradiance, was seen to strongly affect temperature rise, with a computed temperature of 7.5 degrees C for a 1 second pulse at 2 Watts.
Axial refractive index (Figure 7a) change was calculated from axial temperature change. This axial refractive index was scaled to get optical path length. The optical path length difference between temperature at zero time and at a given following the start of the laser pulse was integrated to get a phase change (Figure 7b). These phase changes were plotted as a function of time for various sample thicknesses and beam energies. Longer pulse durations of higher energy at great thicknesses show the greatest amount of phase change, possibly indicating stronger thermal lensing in a media under these conditions.

The damage calculations (Figure 8) demonstrated that radial diffusion plays a larger role in heat transfer loss for smaller beams. More power density is required to achieve a temperature rise sufficient for damage. The effect of radial diffusion was lessened for a larger beam diameter and damage thresholds as a function of beam diameter became relatively constant for constant exposure times.

The collimated geometry could be compared more closely with the experimental data and computed thermal and dn/dT data. The focused geometry was more representative of the actual geometry of the eye, which alters the damage thresholds since stronger focus

increases irradiance, which increases temperature in the eye. The damage irradiance thresholds were lower for focused geometries by 1 and 2 W/cm^2 for a 2.7 mm and 7.1 mm beam, respectively.

VI: Conclusion

A background study was done on previous work in thermal lensing, refractive index shift, and laser-tissue interaction. Physics of a photothermal response and principals of the computational software BTEC were described. An experimental system to measure photothermal interaction in water was constructed and calibrated. Temperature rise in water was measured with a thermal camera for 1200, 1310 and 1318-nm sources, with various beam diameters, power levels, pulse durations, and sample thicknesses. Temperature increases of up to 5 degrees C were seen for a 1 second pulse of 2 Watt, 3.8mm diameter IR radiation at 1318 nm. Iterations of experimental parameters were run in the computational software. Measured and computed maximum temperature rise as function of depth was compared, with strong agreement for larger beam diameters. Maximum back temperature as a function time was also compared between measured and computed, for a 4.4 mm thick sample with quarter-second and one second pulses, at small and large beam diameters. The computed data shows good agreement, with most computed temperatures within 0.5 degrees of the measured temperature. Discrepancies were seen at shallow water depths possibly due to multiple reflections, surface tension effects and radiant emission from the closed shutter, which was back-heated by the laser.

Axial temperature rise was computed for the various beam input parameters. The analysis showed that increased irradiance for a smaller beam was the strongest factor in temperature rise. Refractive index shift and phase shift under beam irradiance were computed. Phase shift was greatest for higher power levels and greater water thicknesses.

Finally, damage power and irradiance thresholds were computed for several pulse durations and beam diameters. When accounting for focused geometry, irradiance damage threshold decreased by about 2 W/cm^2, and power damage threshold decreased by about 0.5 W/cm^2.

VII. Bibliography

[1] Vincelette, R.L. (2009). "Thermal Lensing in Ocular Media". PhD diss., University of Texas at Austin,

[2] Gordon, J.P., R.C. Leite, *et al*. (1965) "Long Transient effects of lasers with inserted liquid samples." Journal of Applied Physics 36(3):3-8

[3] Vincelette, R.L., R. J. Thomas, *et al*. (2009). "First-order model of thermal lensing in a virtual eye." Journal of the Optical Society of America A 26(3):548-558

[4] Kim, J., J.H. Oh and T. E. Milner (2006). "Measurement of optical path length change following pulsed laser irradiation using differential phase optical coherence tomography," Journal of Biomedical Optics 11(4)

[5] Westheimer, G. (1980). The Eye: Including central nervous system control of eye movements. St. Louis, MO, C.V. Mosby Company.

[6] Zuclich, J.A., D.J. Lund and B.E. Stuck (2007). "Wavelength dependence of ocular damage thresholds in the near-IR to far-IR transistion region: Proposed revisions to MPEs," Health Physics 92(1), 12-23

[7] Gobin, A.M., D.P. O'Neal, *et al.* (2005). "Near infrared laser-tissue welding using nanoshells as an exogenous absorber," Lasers in Surgery and Medicine 37(2): 123-129

[8] Sheldon, S.J., L.V. Knight and J.M. Thorne (1982). "Laser-induced thermal lens effect: a new theoretical model," Optical Society of America 21(9): 1663-1669

[9] Irvin, L.J., R. J. Thomas, *et al.* (2007). "BTEC Thermal Model." Interim technical report number AFRL-RH-TR-2008-0006, Brooks-City-Base, TX, Air Force Research Laboratory